Nanotailored Crystalline Morphology in Hexagonally Perforated Layers of a Self-Assembled PS-*b*-PEO Diblock Copolymer

Lei Zhu, Ping Huang, William Y. Chen, Qing Ge, Roderic P. Quirk, and Stephen Z. D. Cheng*

Maurice Morton Institute and Department of Polymer Science, The University of Akron, Akron, Ohio 44325-3909

Edwin L. Thomas

Department of Materials Science and Engineering, Massachusetts Institute and Technology, Cambridge, Massachusetts 02139

Bernard Lotz

Institute Charles Sadron, 6 Rue Boussingault, Strasbourg 67083, France

Benjamin S. Hsiao, Fengji Yeh, and Lizhi Liu

Department of Chemistry, The State University of New York at Stony Brook, Stony Brook, New York 11794-3400

Received December 17, 2001; Revised Manuscript Received February 19, 2002

ABSTRACT: Nanoscale tailored polymer crystalline morphology is studied in a polystyrene-*b*-poly(ethylene oxide) (PS-*b*-PEO) diblock copolymer with number-average molecular weights for the PS and PEO blocks being 17 000 and 11 000 g/mol, respectively. The PEO volume fraction is 0.39. After large amplitude planar reciprocating shear, a hexagonally perforated layer (HPL) structure is obtained. Since the glass transition temperature of the PS blocks (72 °C) is higher than the PEO crystal melting temperature (∼51 °C when the crystallization temperature, T_c, is lower than 40 °C), the PEO block crystallization is confined within the HPL structure. The PEO crystal (the *c* axis) orientation within this complex confined environment is investigated using simultaneous synchrotron two-dimensional small-angle and wide-angle X-ray scattering (SAXS and WAXS) methods. The PEO crystal orientations with respect to the layer plane (or the {000*l*}) of the HPL structure have been found to be dependent upon T_c. At very low T_cs (below −50 °C), the PEO crystals have a random orientation. Between $-50\ °C \le T_c \le -10\ °C$, the PEO crystal *c* axes preferentially orient parallel to the layer plane. Above $T_c = 0$ °C, the crystal *c* axes orient inclined to the layer plane of the HPL structure, and the tilt angle with respect to the layer plane increases with T_c. Contrary to the confined polymer crystallization in nanolamellar structure, however, the *c* axis orientation perpendicular to the layer plane is not found at least up to $T_c = 40$ °C in this HPL confined environment. Meanwhile, the ribbonlike PEO crystal growth is specifically tailored along the {10$\bar{1}$0} planes of the hexagonal PS perforations. Apparent crystallite size analyses using the Scherrer equation confirm the one-dimensional crystal growth at high T_cs. Using time-resolved WAXS experiments, the crystal orientation is observed to occur in the early stage of crystallization with a crystallinity of ∼7 wt %. Based on the results of specifically designed self-seeding experiment, the crystal orientation is determined by the crystal growth (surface nucleation) in the confined HPL phase rather than the preorientation of primary nuclei.

Introduction

Phase and crystallization behaviors in amorphous−crystalline block copolymers have received substantial attention due to hierarchical molecular and supramolecular orderings on different length scales in one system.[1] It has been recognized that three physical events compete with each other or override one over another in forming the final phase and crystalline morphologies in amorphous−crystalline block copolymers, i.e., the microphase separation of the diblock copolymer, the crystallization of the crystallizable blocks, and the vitrification of the amorphous blocks. Accordingly, three temperature parameters associated with these physical events are the order−disorder transition temperature of the diblock copolymer (T_{ODT}), the crystallization temperature of the crystallizable blocks (T_c^c), and the glass transition temperature of the amorphous blocks (T_g^a).[2] Both unconfined and confined crystallizations have been observed in amorphous−crystalline diblock copolymers. For unconfined crystallizations, the crystallization of the crystallizable blocks overrides the preexisting ordered phase morphology of the block copolymers, resulting in an alternating crystalline and amorphous lamellar morphology.[2−16] For confined crystallizations in ordered phase morphologies, two cases have been identified. The first and obvious case is $T_{ODT} > T_g^a > T_c^c$.[16−26] The crystallization of crystallizable blocks is completely confined within the preexisting phase morphologies by the glassy amorphous phase. The second case is less obvious when $T_{ODT} \gg T_c^c > \sim T_g^a$.[7,15,27−31] Although the T_g^a of amorphous blocks is lower than the T_c^c of crystallizable blocks, the confined crystallization may still take place due to a relatively

* To whom correspondence should be addressed. E-mail: cheng@polymer.uakron.edu.

10.1021/ma012184n CCC: $22.00
Published on Web 03/27/2002

Table 1. Molecular Characterization Data of the PS-*b*-PEO Diblock Copolymer Sample

sample	M_n^{PS} (g/mol)[a]	M_n^{PEO} (g/mol)[b]	M_w/M_n[c]	f_{PEO}[d]	T_g^{PS} (°C)[e]	T_m^{PEO} (°C)[f]	T_{ODT} (°C)[g]
PS-*b*-PEO	17 000	11 000	1.09	0.39	72	~51	~210

[a] Determined by size exclusion chromatography calibrated by PS standards. [b] Determined by ^{1}H nuclear magnetic resonance. [c] Determined by SEC using universal calibration. [d] The densities of amorphous PEO and PS at 60 °C are 1.092 and 1.035 g/cm^3.[24] [e] Determined by DSC with a scan rate of 5 °C/min. [f] Determined as peak temperature by DSC for T_c less than 40 °C. [g] Determined by temperature-dependent SAXS experiments.

fast crystallization rate and a low molecular mobility of strongly segregated block copolymers.

Recently, crystal orientations dictated by ordered microdomains in amorphous−crystalline block copolymers have been investigated. These phase morphologies include conventional lamellae,[18−25,27,32−37] hexagonal cylinders (the crystallizable blocks form the cylinders),[28−30,37] and inverse hexagonal cylinders (the crystallizable blocks form the matrix).[38,39] When the crystallizable blocks crystallize in the lamellar phase, two extremes of crystal (the *c* axis) orientations in chain-folded crystals with respect to the lamellar layer surface have been found. Namely, the chain direction is oriented either parallel (a homogeneous configuration)[18,19,21,22,27,37] or perpendicular (a homeotropic configuration) to the layer surface.[32−36] A tilted *c* axis orientation with respect to the layer surface is also proposed for certain lamella-forming block copolymers.[40−42] Different crystal orientations have been speculated to be originated from various block copolymers with different molecular weights.[21,22] A systematic study has recently shown that all types of crystal orientations are observed in a lamellar polystyrene-*b*-poly(ethylene oxide) (PS-*b*-PEO) diblock copolymer, and they are simply dependent upon the crystallization temperature, T_c.[23] When the PS-*b*-PEO samples are quickly quenched into liquid nitrogen from the melt, the PEO crystals adopt random orientations. At low, intermediate, and high T_cs, homogeneous, inclined, and homeotropic crystal orientations with respect to layer surface are observed, respectively. Specific crystal orientations are found to be determined in the initial stage of PEO crystal growth rather than by the preorientation of the primary nuclei within this one-dimensionally (1D) confined lamellae.[25]

The crystal *c* axes in confined cylinders have also been observed to possess different orientations with respect to the cylinder axes.[28−30,37] In most cases, the *c* axes of polyethylene (PE) crystals are found to be either perpendicular or slightly tilted (<30°) from the cylinder axes in two PE-containing diblock copolymers.[28−30] It is speculated that the perpendicular crystal orientation results from a fast crystal growth along the *b* axes of PE crystals in the cylinder-axis direction. We have recently found T_c-dependent crystal orientations in nanocylinders of a PS-*b*-PEO/PS blend.[43] With increasing T_c, the crystal (*c* axis) orientation changes from random to inclined and finally to perpendicular to the cylinder axes. Crystal orientation directed by hexagonal cylinders of the amorphous blocks in the inverse cylindrical phase has also been investigated in PE-containing block copolymers. The *b* axes of PE crystals are oriented more or less parallel to the cylinder axes.[38,39] The *c* axes of PE crystals are perpendicular to the cylinder axes in one PE-containing terpolymer,[38] while they have been further proposed to be parallel to the $\{10\bar{1}0\}$ planes of the inverse cylinders in other two PE-containing diblock copolymers.[39]

Scheme 1. Schematic Representation of the Shear Geometry for the PS-*b*-PEO Sample

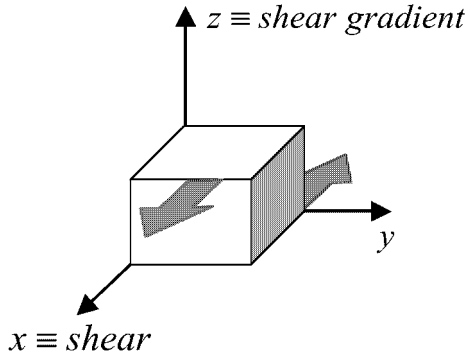

However, research on crystallization and crystal orientations confined within complex phase morphologies has been just started. In this publication, we report our efforts in this area. A PS-*b*-PEO diblock copolymer having $\bar{M}_n^{PS}$ = 17K g/mol and $\bar{M}_n^{PEO}$ = 11K g/mol has been synthesized, and the volume fraction of the PEO blocks is 0.39. After mechanical shear on the microphase-separated samples in the melt, a long-range-ordered hexagonally perforated layer (HPL) structure is obtained.[44] Since the T_g^{PS} of the PS blocks (72 °C) is higher than the melting temperature of the PEO blocks (T_m^{PEO} ~ 51 °C for T_c < 40 °C), the PEO block crystallization is completely confined within the shear-induced HPL structure. Simultaneous two-dimensional (2D) small-angle and wide-angle X-ray scatterings (SAXS and WAXS) have been employed to investigate the PEO crystal orientations and their T_c dependence under the HPL confinement.

Experimental Section

Materials and Sample Preparation. The PS-*b*-PEO diblock copolymer was synthesized via sequential anionic block copolymerization of styrene and ethylene oxide. Detailed synthesis procedures can be found elsewhere.[24] The molecular characterization data for this diblock copolymer are summarized in Table 1.

To ensure the consistency of the phase behavior, uniform sample preparation procedure and thermal history were maintained. The sample was cast from a 5% (w/v) toluene solution, and the solvent was allowed to evaporate slowly under a dry nitrogen atmosphere at 50 °C to prevent the crystallization of the PEO blocks. Residual solvent was removed under vacuum at 50 °C for 1 day, and the sample was then annealed at 100 °C for 12 h to allow the development of microphase separation. To study the crystal orientation, the microphase-separated samples were subjected to large-amplitude reciprocating planar shear under a dry argon atmosphere at 120 °C, using a laboratory-built shear apparatus. The shear frequency was 0.5 Hz, and the shear amplitude was 150%. The shear direction was along the *x* direction, and the shear gradient was along the *z* direction, as shown in Scheme 1. Therefore, the shear plane was the *xy* plane. The shear-oriented samples were further annealed at 100 °C for another 12 h in a vacuum to eliminate any residual stresses.

Equipment and Experiments. Simultaneous 2D SAXS and WAXS experiments were conducted at the synchrotron

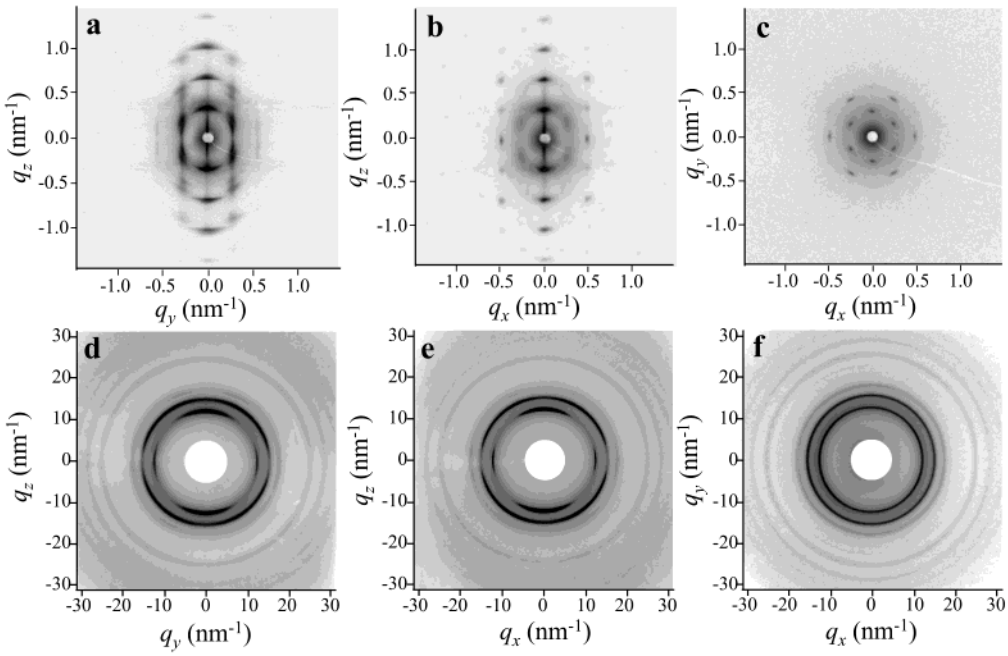

Figure 1. X-ray scattering patterns of shear-aligned PS-*b*-PEO (17K−11K) sample isothermally crystallized at −10 °C. (a) and (d) are 2D SAXS and WAXS patterns obtained when the X-ray beam is parallel to the *x* direction; (b) and (e) are 2D SAXS and WAXS patterns along the *y* direction; (c) and (f) are 2D SAXS and WAXS patterns along the *z* direction.

X-ray beamline X27C at the National Synchrotron Light Source in Brookhaven National Laboratory. The wavelength (λ) of the X-ray beam was 0.1307 nm. The center of the 2D SAXS pattern was calibrated using silver behenate, with the first-order scattering vector q ($q = 4\pi \sin\theta/\lambda$, where 2θ is the scattering angle) being 1.076 nm^{-1}. 2D WAXS was calibrated using α-Al_2O_3 with known crystal diffractions. Air scattering was subtracted for both 2D SAXS and WAXS. Azimuthal profiles for 2D WAXS patterns were obtained via scans, starting on the vertical direction of the patterns. The standard deviation of determining the angular maximum was ±3°.

To analyze the correlation lengths (apparent crystallite sizes), the Scherrer equation was used:

$$D_{hkl} = \frac{K\lambda}{\beta_{hkl}\cos\theta} \tag{1}$$

where D_{hkl} was the mean crystallite size along the [hkl] direction and K was the shape factor (the Scherrer constant, and a value of 0.94 was used in this case[45]). β_{hkl} was the pure line breadth and θ the half-scattering angle. Usually, β_{hkl} was taken as the half-width of the (hkl) diffraction. Assuming that the diffraction peak shape obeyed a Gaussian function, Warren's correction can be used to correct instrument broadening:[45]

$$\frac{\beta_{hkl}}{B_{hkl}} = \sqrt{1 - \frac{b^2}{B_{hkl}^2}} \tag{2}$$

where B_{hkl} was the experimentally observed full width at half-maximum (fwhm) of the diffraction peak and b was the fwhm of a standard specimen diffraction. To ensure a good calibration, the mean crystallite size of the standard specimen should be over 60 nm. The quartz line at 60.0° was taken for standard b.

Isothermal crystallization experiments were conducted using an Instec LN2-P2 hot stage equipped with a liquid nitrogen cooling system. The isothermal T_c was controlled to within ±0.2 °C. The shear-aligned samples were preheated to 70 °C on another hot stage for 3 min in a dry nitrogen atmosphere and then quickly quenched (switched) to the hot stage with a preset T_c for crystallization.

Results and Discussion

Simultaneous 2D SAXS and WAXS for the Crystal Orientation Study in the Shear-Induced HPL Confinement. The phase structure and orientation information on the sheared-aligned sample can be obtained from 2D SAXS results, and the PEO crystal orientation can be identified from 2D WAXS results. Figure 1a−f shows 2D SAXS and WAXS results on the sheared PS-*b*-PEO sample as the incident X-ray beam along three orthogonal (*x*, *y*, and *z*) directions (see Scheme 1). The T_c for the sample shown in these figures is −10 °C. From the SAXS results, ordered HPL diffraction patterns are evident.[44] The SAXS pattern along the *z* direction (Figure 1c) shows clear 6-fold symmetry, indicating that the PS perforations within the PEO layers pack into a long-range-ordered 2D hexagonal lattice. On the other hand, the layer reflections are seen on the meridian in the SAXS patterns along both the *x* and *y* directions in Figure 1a,b. However, the SAXS patterns along the *x* and *y* directions show distinctive reflections, indicating that after mechanical shear a "single-crystal"-like diblock copolymer sample has been obtained.[44] Through detailed analysis, different SAXS patterns in Figure 1a,b can be identified as the incident X-ray beam along an apex and a side of a hexagonal lattice. The shear-induced HPL structural determination has been described elsewhere using systematic crystallographic analyses based on the SAXS and transmission electron microscopy (TEM) results.[44] It has been found that the HPL structure is a mixture of trigonal ($R\bar{3}m$) twins and a hexagonal ($P6_3/mmc$) structure, with trigonal twins being the major components. Edge dislocations (stacking faults) formed during plastic deformation have been found to control the unique HPL structure.[44] From the SAXS data in Figure 1, the overall layer thickness ($d = d_{PEO} + d_{PS}$) is 18.9 nm, and the distance between neighboring PS perforation centers within the PEO layer is $D_{PS-PS} = 26.6$ nm. Combining the TEM and SAXS results and the volume fraction of the PEO blocks, the thicknesses of the PS and PEO

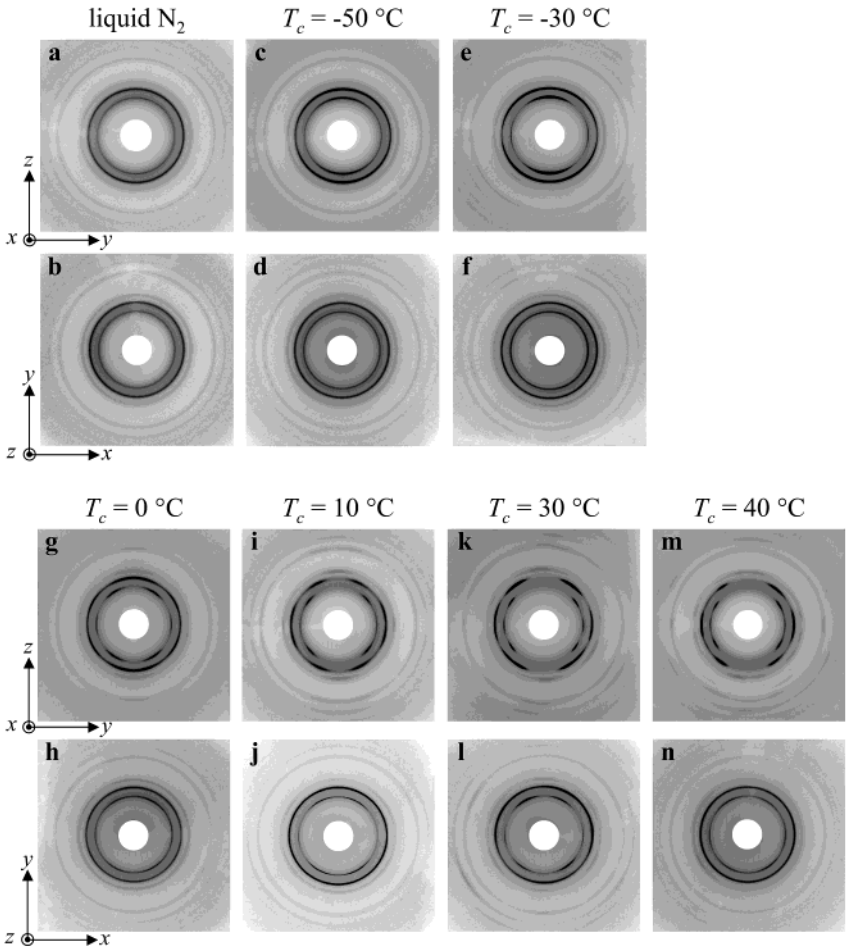

Figure 2. WAXS patterns along the *x* (top) and *z* (bottom) directions of shear-aligned PS-*b*-PEO (17K−11K) sample quickly quenched to a preset T_c from the melt at 70 °C: (a, b) liquid nitrogen; (c, d) −50 °C; (e, f) −30 °C; (g, h) 0 °C; (i, j) 10 °C; (k, l) 30 °C; and (m, n) 40 °C.

layers are $d_{PS} = 9.9$ nm and $d_{PEO} = 9.0$ nm, respectively. The average diameter of the PS perforations is $D_{PS} = 12.2$ nm. Therefore, in this HPL structure the monocontinuous PS microdomain constructs complex nanocompartments for the PEO block crystallization after the vitrification of the PS phase. Note that the T_g^{PS} (72 °C) is higher than the T_m^{PEO} (∼ 51 °C when $T_c^{PEO} < 40$ °C), as shown in Table 1.

The corresponding 2D WAXS along the *x*, *y*, and *z* directions are shown in Figure 1d−f. The 2D WAXS patterns obtained along both the *x* and *y* directions are identical, while that along the *z* direction is different. This phenomenon has been observed for the samples isothermally crystallized at other T_cs. Since we focus on the PEO crystal orientation in the HPL confinement in this publication, only the X-ray patterns along the *x* and *z* directions are used for the following discussion.

Crystal Orientations in the HPL Confinement at Different T_cs. In general cases, PEO homopolymer crystallizes into a monoclinic crystalline structure with a distorted $^7/_2$ helix chain conformation. The monoclinic unit cell of PEO crystals has parameters of $a = 0.805$ nm, $b = 1.304$ nm, $c = 1.948$ nm, and $\beta = 125.4°$, and the space group is $P2_1/a$-C_{2h}^5.[46] The PEO crystal reciprocal lattice and its diffraction properties, which are important for analyzing the PEO crystal orientation in the shear-induced HPL confinement, have been reviewed in ref 23.

The shear-aligned sample is quickly quenched to a preset T_c from the melt (held at 70 °C for 3 min). After the crystallization of the PEO blocks, the 2D SAXS patterns are always the same as those shown in Figure 1a−c, indicating that the HPL structure is kept after the PEO block crystallization. However, the 2D WAXS patterns along the *x* and *z* directions are different at different T_cs (Figure 2). As shown in Figure 2a,b, when the sample is quickly quenched into liquid nitrogen [we estimate that the crystallization takes place between the T_g^{PEO} (∼−70 °C) and −50 °C], both the 2D WAXS patterns along the *x* and *z* directions exhibit isotropic (ring) reflections, indicating a random crystal orientation in the HPL confinement. During this quenching process, a large number of primary nucleation sites are created. It is speculated that the nucleation density is so high that the neighboring nuclei quickly impinge with one another, and little crystal growth is needed to complete the crystallization. In other words, the randomly oriented PEO crystals are substantially smaller than the PEO layer thickness of 9.0 nm along the *z* direction and the interstices of 14.4 nm ($D_{PS-PS} - D_{PS} = 26.6-12.2$ nm) between neighboring PS perforations in the *xy* plane. Therefore, they cannot "feel" the confinement provided by the glassy PS compartments.

When the sample is quickly quenched from the melt to temperatures between −50 and −10 °C, the 2D WAXS patterns along the *x* and *z* directions are shown in Figures 2c−f and 1d,f. Since the 2D WAXS patterns along the *z* direction in Figures 2d,f and 1f show isotropic rings, the *c* axes of PEO crystals are macroscopically isotropic with respect to the *z* direction in this

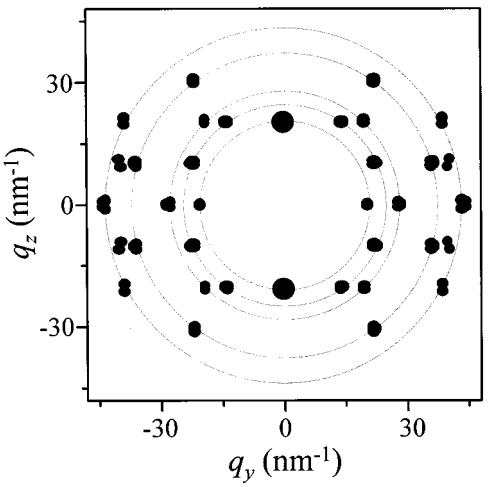

Figure 3. Calculated PEO [120] uniaxial pattern. The first reflection ring is the (120) reflections. The second ring includes the ($\bar{1}32$), (032), ($\bar{2}12$), (112), ($\bar{1}24$), ($\bar{2}04$), and (004) reflections. The third ring includes the ($\bar{2}24$) and ($\bar{0}24$) reflections. The fourth ring includes the ($\bar{3}24$), (124), ($\bar{2}44$), and (044) reflections. The fifth ring includes the ($\bar{3}28$)and ($\bar{1}28$) reflections. The ($\bar{1}08$) and ($\bar{3}08$) reflections are in between the forth and fifth rings but closer to the fifth ring.

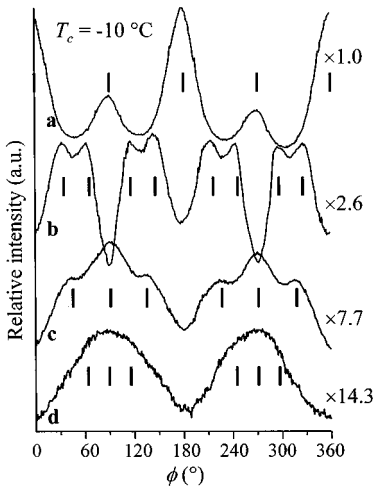

Figure 4. Azimuthal scanning profiles of the (a) first ring, (b) second ring, (c) third ring, and (d) fifth ring reflections of the WAXS patterns in Figure 1d for the PS-*b*-PEO (17K−11K) sample isothermally crystallized at $T_c = -10$ °C. The intensity magnifications are indicated on the right of the azimuthal profiles. The short vertical bars indicate positions of the predicted reflections in the [120] uniaxial pattern in Figure 3.

T_c region. However, the 2D WAXS patterns obtained along the *x* direction in Figures 2c,e and 1d exhibit clear orientation of the (120) reflections (*d* spacing = 0.463 nm) with major intensity along the *z* direction and minor intensity in the *xy* plane. The overlapped reflections on the second reflection ring in these 2D WAXS patterns are oriented in the quadrants.

These experimental diffraction patterns observed can be quantitatively explained using a PEO [120] uniaxial pattern with the [120] direction parallel to the *z* direction,[23] which is shown in Figure 3. Based on this [120] uniaxial pattern, four (120) reflections are on the first reflection ring, with the intensities on the meridian stronger than those on the equator. The (120) reflections in the 2D WAXS patterns along the *x* direction in Figures 2c,e and 1d show that, with increasing T_c, the orientation of the (120) reflections progressively improves. The azimuthal scanning profile of the first reflection ring in Figure 1d at $T_c = -10$ °C shows that two sets of the (120) reflections are 90° apart from each other, with one set at $\phi = 0°$ and 180° stronger than those at $\phi = 90°$ and 270°. This is illustrated in Figure 4a and is consistent with the calculated [120] uniaxial diffraction pattern in Figure 3.

In the [120] uniaxial pattern (see Figure 3), eight reflections on the second reflection ring (*d* spacing = 0.39 nm) are calculated to be at $\phi = 35°$, 65°, 115°, 145°, 215°, 245°, 295°, and 325°. The second ring reflections in the 2D WAXS patterns along the *x* direction in Figures 2c,e and 1d indicate that the orientation of the overlapped reflections also enhances with increasing T_c. The azimuthal scanning profile of the second reflection ring in Figure 1d at $T_c = -10$ °C exhibits that eight reflections are located at $\phi = 34°$, 63°, 117°, 145°, 214°, 244°, 295°, and 326° (Figure 4b), and they fit well with the calculated [120] uniaxial pattern. Note that slight misalignment of the sample may cause intensity changes in addition to the contributions of individual structural factors in these overlapped reflections. Therefore, we only focus on the reflection positions.

Figure 3 also indicates six reflections on the third reflection ring (*d* spacing of 0.34 nm) at $\phi = 44°$, 90°, 136°, 224°, 270°, and 316°. At $T_c = -10$ °C, there are six maxima at $\phi = 45°$, 91°, 135°, 227°, 270°, and 316° (Figure 4c), based on the azimuthal scanning profile of the third reflection ring in Figure 1d, and they fit well with the calculated [120] uniaxial pattern.

The question now is whether we can determine that the experimentally observed WAXS patterns in Figures 2c,e and 1d correspond to the pure [120] uniaxial pattern or a mixture of the [120] uniaxial and the *c* uniaxial (fiber) patterns. This problem cannot be solved until we examine the reflections on the fifth reflection ring (*d* spacing = 0.22 nm). The [120] uniaxial pattern in Figure 3 predicts six reflections at $\phi = 62°$, 90°, 118°, 242°, 270°, and 298°. The azimuthal scanning profiles of the fifth reflection ring in the experimental 2D WAXS patterns along the *x* direction in Figures 2c,e and 1d are carried out. Figure 4d shows an example at $T_c = -10$ °C (Figure 1d) that the reflections at 62°, 90°, and 118° merge into a broad reflection centered around 90°, and the reflections at 242°, 270°, and 298° merge into another broad reflection centered around 270°. No major reflections are found at $\phi = 28°$, 152°, 208°, and 332°, which are characteristics of the PEO crystal reflections on the fifth reflection ring in the *c* uniaxial pattern.[23] Therefore, we conclude that the WAXS patterns in Figures 2c,e and 1d can be explained using a pure [120] uniaxial pattern, rather than a mixture of the [120] uniaxial and the *c* uniaxial patterns. It is thus deduced that the PEO crystal *c* axes are preferentially oriented parallel to the layer plane (the {000*l*}) of the HPL structure.

A real space model for the PEO crystal orientation between -50 °C $\leq T_c \leq -10$ °C in the HPL confinement is shown in Figure 5. From the top view (along the *z* direction) of the HPL structure, the PS perforations form a hexagonal array within the PEO layer, and a cross-section view along the OO′ line is shown at the bottom. Based on our TEM[44] and a previous report,[47] the shape of the PS perforations may deviate from the cylinder shape, and a "hourglass" shape is used in this real space model. Assuming that the *c* axes of the PEO crystals are perpendicular to the *z* direction and ran-

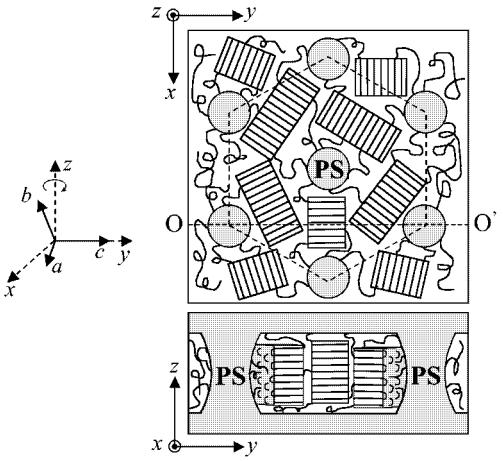

Figure 5. Schematic of the PEO crystal orientation within one layer of the confined HPL structure. The upper part shows a top view along the normal of the HPL layer plane (through the *z* direction), and the cross-section view at the OO′ line is shown at the bottom (through the *x* direction). The PEO crystal unit cell is defined by *a*, *b*, and *c*.

domly oriented in the *xy* plane, isotropic ring reflections in the 2D WAXS pattern along the *z* direction (see Figures 2d,f and 1f) are achieved. The *b* axes of the PEO crystals thus have to tilt 45° from the *xy* plane. Note that a pair of the [120] directions, which are the fast crystal growth directions in the PEO crystallization,[48,49] is in the *xy* plane (see Figures 2c,e and 1d). The random orientation of PEO crystals around the *z* axis in Figures 2d,f and 1f implies that these crystals are "confined" in the hexagonal cell constructed by the PS perforations (see the dashed-line hexagon in Figure 5). Therefore, the upper limit of the in-plane lateral sizes of the PEO lamellar crystals along one [120] direction (see the top view in Figure 5) is estimated to be $2d_{10\bar{1}0} - D_{PS} = 33.9$ nm, while the upper limit of the out-of-plane lateral sizes of the PEO lamellar crystals along the other [120] direction (see the cross-section view in Figure 5) is 9.0 nm. This nanoconfined PEO crystallization can be attributed to high nucleation densities and thus small crystal sizes at relatively low T_cs (-50 °C $\leq T_c \leq -10$ °C), as shown in Figure 5.

The 2D WAXS patterns along the *x* and *z* directions for the sheared sample crystallized at 0 °C $\leq T_c \leq$ 40 °C are shown in Figure 2g−n. In the 2D WAXS patterns along the *x* direction, the sharp (120) reflections in the *xy* plane remain while those on the *z* direction split and gradually move toward the *xy* plane with increasing T_c. As a result, two pairs of the (120) reflections appear in the quadrants. These diffraction patterns can be explained with tilted crystal orientations in the HPL confinement. We define that the tilt angle is between the crystal *c* axes and the layer plane (the {000*l*}). To quantitatively analyze the diffraction patterns with a tilted *c* axis orientation, we chose the experimental results observed at $T_c = 0$ °C (Figure 2g), where the *c* axes of PEO crystals tilt 34° from the HPL layer plane. We thus construct a $\hat{n}_{34°}$ uniaxial diffraction pattern for the PEO crystals as shown in Figure 6. In this figure, six (120) reflections on the first reflection ring are predicted at ϕ = 34°, 90°, 146°, 214°, 270°, and 326°. The azimuthal scanning profile of the first reflection ring of Figure 2g at this T_c shows six maxima at 36°, 89°, 148°, 218°, 271°, and 328° (Figure 7a) and are consistent with those in the calculated $\hat{n}_{34°}$ uniaxial pattern. With increasing T_c, the four (120) reflections

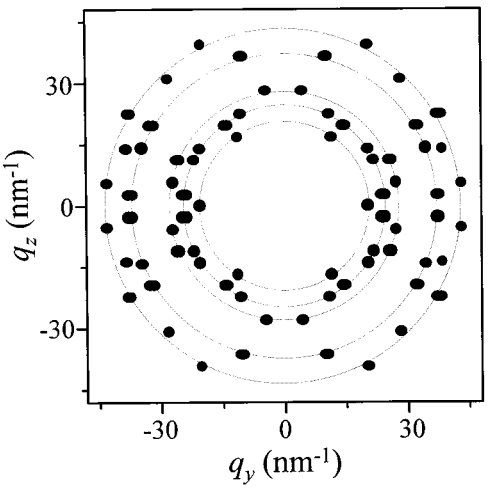

Figure 6. Calculated PEO $\hat{n}_{34°}$ uniaxial pattern. The (120) reflections are on the first ring. The ($\bar{1}32$), (032), ($\bar{2}12$), (112), ($\bar{1}24$), ($\bar{2}04$), and (004) reflections are on the second ring. The ($\bar{2}24$) and (024) reflections are on the third ring. The (124), ($\bar{3}24$), (044), and ($\bar{2}44$) reflections are on the fourth ring. The ($\bar{3}28$) and ($\bar{1}28$) are on the fifth ring. The ($\bar{1}08$) and ($\bar{3}08$) reflections are in between the forth and fifth rings but closer to the fifth ring.

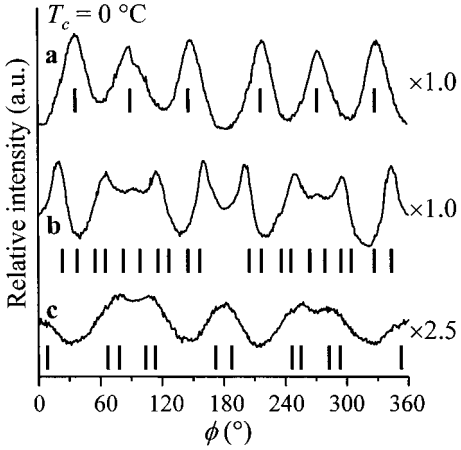

Figure 7. Azimuthal scanning profiles of the (a) first ring, (b) second ring, and (c) third ring reflections of the WAXS patterns in Figure 2g for the PS-*b*-PEO (17K−11K) sample isothermally crystallized at $T_c = 0$ °C. The intensity magnifications are indicated on the right of the azimuthal profiles. The short vertical bars indicate positions of the predicted reflections in the $\hat{n}_{34°}$ uniaxial pattern in Figure 6.

in the quadrants gradually move toward the *xy* plane (Figure 2i,k,m), revealing an increase of the tilt angle from the layer plane.

The azimuthal scanning profile of the second ring in the WAXS patterns along the *x* direction at $T_c = 0$ °C (Figure 2g) is shown in Figure 7b. In Figure 6, there are 20 reflections on the second reflection ring at ϕ = 26°, 36°, 56°, 63°, 83°, 97°, 117°, 124°, 144°, 154°, 206°, 216°, 236°, 243°, 263°, 277°, 297°, 304°, 324°, and 334° (vertical bars in Figure 7b). The azimuthal scanning profile of the second reflection ring at $T_c = 0$ °C shows 10 maxima which fit the $\hat{n}_{34°}$ uniaxial pattern with every two calculated neighboring reflections overlapping into one maximum (Figure 7b). With increasing T_c, these reflections gradually merge into six maxima due to the tilt angle increase from the *xy* plane (Figure 2i,k,m).

The azimuthal scanning profile of the reflections on the third reflection ring in Figure 2g at $T_c = 0$ °C is shown in Figure 7c. In Figure 6, 12 reflections are

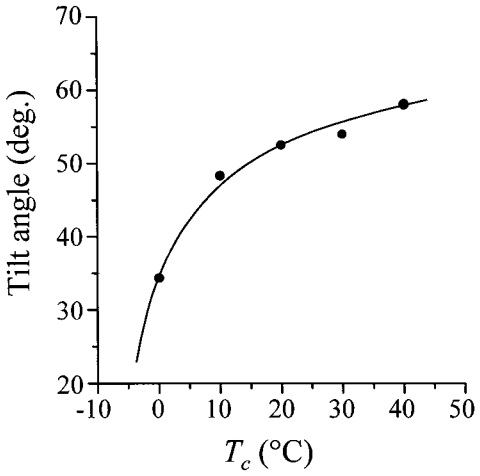

Figure 8. The *c* axis tilt angle dependence on the T_c. The tilt angle is between the PEO crystal *c* axes and the {000*l*} layer plane of the HPL structure.

predicted on the third reflection ring at $\phi = 9°$, 67°, 78°, 102°, 114°, 171°, 189°, 247°, 258°, 282°, 293°, and 351° in the $\hat{n}_{34°}$ uniaxial pattern (vertical bars in Figure 7c). In Figure 7c, every two calculated reflections in the $\hat{n}_{34°}$ uniaxial pattern merge into one maximum, and all together six maxima centered at $\phi = 0°$, 79°, 108°, 180°, 255°, and 282° are observed. Therefore, the experimental data also fit with the calculated $\hat{n}_{34°}$ uniaxial pattern. Note that no major reflections are observed at $\phi = 45°$, 135°, 225°, and 315°, which are the predicted reflections on the third reflection ring of the *c* uniaxial pattern.[23] We thus conclude that the 2D WAXS pattern at $T_c = 0$ °C represents a pure 34° tilt angle uniaxial pattern, rather than a mixture of the tilt axis uniaxial and the *c* uniaxial patterns. These X-ray analyses demonstrate that in the PEO crystals the *c* axes preferentially orient inclined to the layer plane of the HPL structure in the temperature region between 0 and 40 °C. This is different from the observations of the PEO crystal orientation in nanolamellar confinement where the *c* axes of PEO crystals are observed perpendicular to the layer plane for $T_c \geq 35$ °C.[23] A quantitative plot of the *c* axis tilt angle of the PEO crystals from the layer plane in the HPL confinement at different T_cs is shown in Figure 8. The tilt angle increases with T_c and levels off at ~55°−60° above $T_c = 20$ °C. It is speculated that as a compromise of the tethered PEO blocks in both the PS layers and perforations (see Figure 10), the PEO crystal orientation has to be inclined, and the perpendicular crystal orientation with respect to the layer plane of the HPL structure may not be favorable.

Furthermore, it is particularly interesting that the 2D WAXS patterns along the *z* direction between 0 °C $\leq T_c \leq$ 40 °C (Figure 2h,j,l,n) no longer show random crystal orientation as seen for −50 °C $\leq T_c \leq$ −10 °C. The azimuthal scanning profiles for the first (120) reflection ring in the WAXS patterns along the *z* direction are shown in Figure 9. Six maxima are observed at around $\phi = 0°$, 60°, 120°, 180°, 240°, 300°, and 360°. (The nonequal intensity may result from slight misalignments of the sample.) This hexagonal symmetry indicates that the inclined PEO ribbonlike crystals in the confined HPL layers preferentially orient into three directions that are 120° apart from each other. Comparing this hexagonal reciprocal lattice in the WAXS patterns with that in the 2D SAXS patterns (Figure 1c), we conclude that the PEO crystal growth

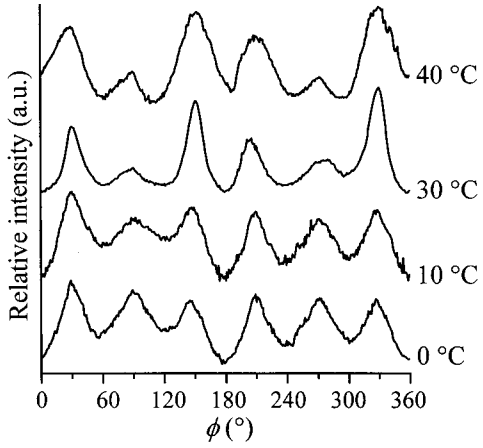

Figure 9. Azimuthal scanning profiles of the (120) reflections on the first (120) reflection ring in the WAXS patterns along *z* (Figure 2h,j,l,n) for the PS-*b*-PEO (17K−11K) sample isothermally crystallized between 0 °C $\leq T_c \leq$ 40 °C.

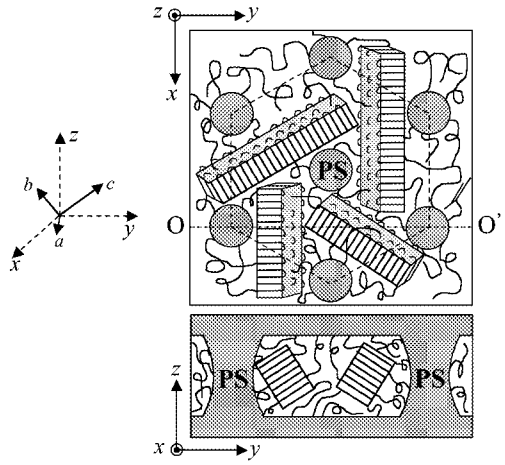

Figure 10. Schematic of the inclined PEO crystal orientation within one layer of the confined HPL structure. The upper part shows a top view along the normal direction of the HPL layer plane (through the *z* direction), and the cross-section view at the OO′ line is shown at the bottom (through the *x* direction). The PEO crystal unit cell is defined by *a*, *b*, and *c*.

is guided along the {10$\bar{1}$0} planes of the hexagonal PS perforations within the PEO layers.

On the basis of these analyses, a real space model for the crystal orientation between 0 °C $\leq T_c \leq$ 40 °C can be schematically shown in Figure 10. The PEO crystal *c* axes are tilted with respect to the layer plane in the HPL confinement (the *xy* plane), as shown in the cross-section view of a HPL layer at OO′. If one views from the top of the HPL structure (along the *z* direction), the PEO lamellar crystal preferentially orient parallel to the {10$\bar{1}$0} planes of the hexagonal PS perforations. It is expected that at these relatively high T_cs the nucleation density is low. An inclined, ribbonlike PEO crystal can grow to a longer distance than the restriction imposed by the PS perforations before the impingement with another PEO crystal. In this case, one [120] direction in the PEO crystal (the fast crystal growth direction) is directed along the tilted direction with respect to the {000*l*} layer plane, and the other is along the {10$\bar{1}$0} planes of the hexagonal PS perforations to avoid the geometric confinement in the HPL structure.

Since the WAXS results represent global crystal orientation in the sample, it is difficult to know if within one PEO layer the lamellar crystals have uniform

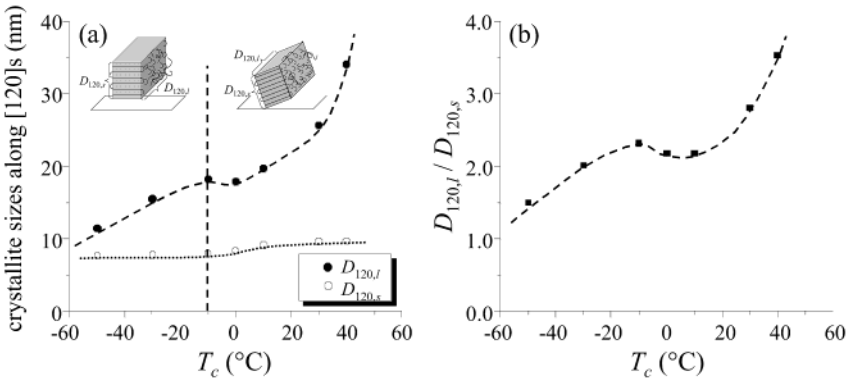

Figure 11. (a) Correlation length (apparent crystallite size) analyses for the (120) reflections in the 2D WAXS patterns along the *x* direction at different T_cs (see Figure 2c−e,g,i,k,m). (b) The ratio of $D_{120,l}/D_{120,s}$ at different T_cs.

orientation (all ribbonlike crystals orient in the same direction), or they have different orientations as shown in Figure 10. If the long, ribbonlike crystals orient in the same direction within one PEO layer, there could leave three uncrystallized (amorphous) parallel "holes" in one hexagonal cell (see dashed line hexagon in Figure 10). Assuming the crystal thickness is around 5−6 nm and the *c* axis tilt angle is 60° (e.g., at $T_c \sim 40$ °C), the crystallinity of the PEO blocks is calculated to be ∼30 wt %. However, if different ribbonlike crystal orientations fill up the hexagonal compartment as shown in Figure 10, the calculated crystallinity of the PEO blocks is ∼50 wt %. This value is close to the DSC and WAXS results that the overall PEO crystallinity at $T_c = 40$ °C is ∼60 wt %. Therefore, it is reasonable to assume that within one PEO layer different orientations of the ribbonlike crystals exist.

Apparent Crystallite Size Estimation Using the Scherrer Equation. To study the crystal growth dimensions within the confined HPL structure, we perform apparent crystallite size (correlation length) analysis on the WAXS patterns along the *x* direction (Figure 2c−e,g,i,k,m) using the Scherrer equation to estimate the correlation length changes along the two [120] directions. As shown in Figure 11a in the region of -50 °C $\leq T_c \leq -10$ °C, the correlation length of the (120) reflection along the *z* direction ($D_{120,s}$) is shorter than that in the *xy* plane ($D_{120,l}$), indicating that the crystal growth in the *xy* plane is less constrained than that along the *z* direction. In this T_c region, the $D_{120,s}$ keeps almost constant at 7.5 nm because of the 1D confinement along the *z* direction, while the $D_{120,l}$ gradually increases because of a decrease in the primary nucleation density of the crystals with increasing T_c. When one makes extrapolations to $T_c = -65$ °C, the $D_{120,s}$ becomes equal to the $D_{120,l}$, indicating an isotropic correlation length of the crystals along both of the [120] directions when $T_c \leq -65$ °C. This is consistent with the observed experimental result when the sample is quickly quenched into liquid nitrogen. Note that the upper limits of the $D_{120,l}$ and the $D_{120,s}$ are estimated to be 33.9 nm ($2d_{10\bar{1}0} - D_{PS}$) and 9.0 nm, respectively (e.g., see Figure 5). Therefore, the calculated $D_{120,s}$ (∼7.5 nm), the correlation length perpendicular to the layer plane, may reflect an actual crystal size. Although the calculated $D_{120,l}$ (the correlation length parallel to the layer plane) reflects merely a lower limit of the actual crystal size in the *xy* plane (i.e., the $D_{120,l}$ actual crystal size in the *xy* plane), the fact that the $D_{120,l}$ between -50 °C $\leq T_c \leq -10$ °C in Figure 11a is much smaller than 33.9 nm is consistent with our previous conclusion that the PEO crystals are "confined" within the hexagonal compartment (cell) of the PS perforations as shown in Figure 5.

When T_c increases from 0 to 40 °C, the *c* axis orientation starts to tilt from the *xy* plane. One can see that there are also two correlation lengths in these two [120] directions (see Figure 2g,i,k,m). One is parallel to the *xy* plane (i.e., $D_{120,l}$ is parallel to the layer plane), and the other is tilted from the plane (i.e., $D_{120,s}$). Above $T_c = 0$ °C, the $D_{120,s}$ slightly increase from 7.5 to 9.0 nm at $T_c = 10$ °C and then levels off at ∼9.6 nm at higher T_cs. Since the PEO *c* axes are still inclined to the layer plane (note that the tilt angle also levels off at ∼60°) even at 40 °C (see Figure 8), the PEO crystal growth along the inclined [120] direction is always confined by neighboring PS layers. For $T_c > 0$ °C the $D_{120,l}$ increases monotonically with increasing T_c. On the other hand, there is a slight decrease in $D_{120,l}$ between -10 °C $< T_c \leq 0$ °C. We speculate that one of the reasons for this $D_{120,l}$ changes between -10 °C $< T_c \leq 0$ °C may be associated with a change of nucleation mechanism from homogeneous to heterogeneous nucleation. It was reported that the homogeneous to heterogeneous nucleation change for a PEO having a $\bar{M}_n$ of about 10K g/mol occurred at a T_c around 0 °C.[50]

If we plot the ratio of $D_{120,l}/D_{120,s}$ vs T_c, the result illustrates an anisotropic crystal growth along both the [120] directions, as shown in Figure 11b. Between -50 °C $\leq T_c \leq -10$ °C, the $D_{120,l}/D_{120,s}$ increases from 1.5 to 2.3, indicating a 1D crystal growth in the confined layer, and the anisotropy of the 1D crystal growth increases with increasing T_c due to a decrease of the primary nucleation density (along the $D_{120,l}$ direction confinement is provided by the impingement with neighboring crystals and/or the PS perforations). Between 0 °C $\leq T_c \leq 10$ °C, there is a minimum in $D_{120,l}/D_{120,s}$ due to a slight decrease in $D_{120,l}$ and a slight increase in $D_{120,s}$ (see Figure 11a). Above $T_c = 10$ °C, $D_{120,l}/D_{120,s}$ continuously increases to 3.5 at 40 °C, indicating an increased anisotropy in the crystal growth in the HPL confinement. For example, at $T_c = 40$ °C the $D_{120,l}$ and $D_{120,s}$ are 34.0 and 9.6 nm, respectively. This is in accordance with the fact that at high T_cs the nanotailored PEO lamellar crystals along the $\{10\bar{1}0\}$ planes of the PS perforations are ribbonlike, as illustrated in Figure 10.

Formation and Determining Factors of the Crystal Orientation during Isothermal Crystallization. Time-resolved simultaneous 2D WAXS and SAXS experiments are conducted to monitor the formation of

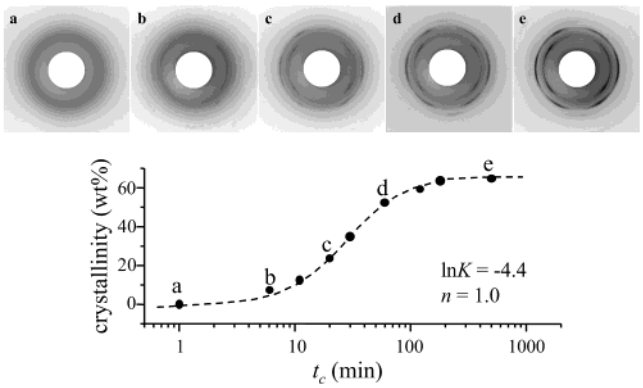

Figure 12. Sets of 2D WAXS patterns along the *x* direction for the shear-aligned PS-*b*-PEO isothermally crystallized at 35 °C for different times. At the bottom shows the crystallinity development with the crystallization time.

crystal orientation within the HPL confinement. Figure 12 shows a series of time-resolved WAXS patterns along the *x* direction at different crystallization time (t_c) at T_c = 35 °C. At t_c = 1 min, an amorphous halo is observed in the 2D WAXS pattern (Figure 12a). At t_c = 6 min, the weak (120) reflections start to be observed in both quadrant and the *xy* plane (even weaker) in the 2D WAXS pattern of Figure 12b, indicating that at this early crystallization stage the tilted crystal orientation has formed. The crystallinity is estimated to be ∼7 wt %. With further increasing the t_c, the crystallinity gradually increases, and the crystal orientation and the orientation distribution do not change throughout the isothermal crystallization process. Therefore, the inclined crystal orientation is formed in an early stage of crystallization with a low crystallinity (∼7 wt %). Subsequent crystallization process is to increase crystallinity without changing the crystal orientation in the system. The overall PEO crystallinity development with t_c can be fitted with the Avrami equation, and the Avrami exponent n = 1.0 and ln K = −4.4 (t_c is in minutes), indicating that the PEO crystal growth is almost 1D if an athermal nucleation mechanism is assumed. This also supports our previous conclusion that the PEO crystal growth is almost 1D and the PEO crystals are ribbonlike at high T_cs.

The early stage crystallization includes two steps: primary nucleation and initial stage of crystal growth (surface nucleation). In a previous study, self-seeded crystallization experiments were used to understand which step determines the crystal orientation.[25] Figure 13 shows the self-seeding experiment results for the confined crystallization in the HPL structure. The idea is to use self-seeds as primary nuclei, and thus, the primary nucleation step can be separated from the subsequent crystal growth. A sample is first isothermally crystallized at T_c = −10 °C. The PEO crystal *c* axes are parallel to the layer plane, and the PEO crystals are randomly oriented within the layer plane (the {000*l*}), as evidenced in the WAXS patterns along the *x* and *z* directions in Figure 13a,b. The sample is then slowly heated at a scanning rate of 1 °C/min to a temperature (58.5 °C) where a very few percent crystallinity is remained to serve as self-seeds (DSC result provides evidence of remaining self-seeds) and is subsequently quenched to a preset T_c of 40 °C and isothermally crystallized there. Note that the inclined crystal orientation forms at this T_c in non-self-seeded crystallization. If the final crystal orientation is identical to

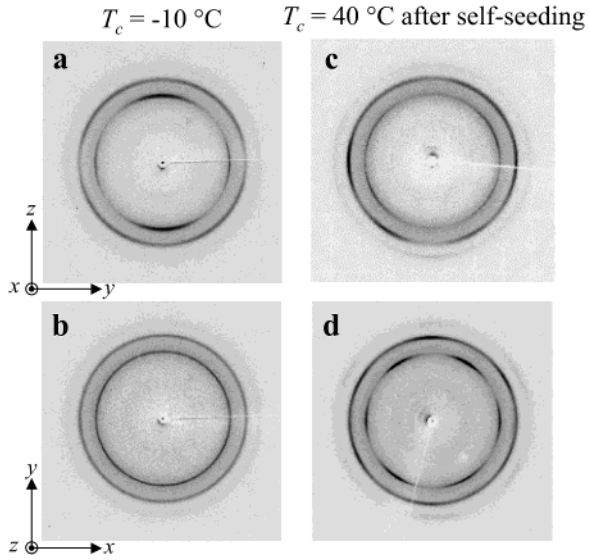

Figure 13. 2D WAXS patterns along the *x* (top) and *z* (bottom) directions for the PS-*b*-PEO sample isothermally crystallized at −10 °C (a, b) and after self-seeded crystallization at 40 °C (c, d).

that in the original isothermal crystallization at T_c = −10 °C (i.e., the *c* axes are parallel to the layer plane), then the orientation of the primary nucleation determines the final crystal orientation. If the final crystal orientation changes to the inclined crystal orientation after the self-seeded crystallization, the primary nucleation is thus not a determining factor for the crystal orientation; rather, the determining step is the initial stage of crystal growth. The WAXS patterns along the *x* and *z* directions showing the crystal orientation after the self-seeded crystallization at 40 °C are given in Figure 13c,d. The results clearly indicate that the original parallel crystal orientation with respect to the layer plane changes to an inclined crystal orientation, and the tilt angle is at ∼56°. In Figure 13d, the perfect 6-fold (120) reflections indicate that the ribbonlike PEO crystal lamellae are now tailored along the {10$\bar{1}$0} planes of the PS perforations. Therefore, we conclude that the formation of specific crystal orientation is determined by the crystal growth step in an early stage of crystallization in the nanoconfined HPL structure.

Conclusion

In summary, we have used combined 2D SAXS and WAXS techniques to study confined PEO block crystallization in an HPL-forming PS-*b*-PEO (17K−11K) diblock copolymer. Experimental results show that the crystal (the *c* axis) orientation is simply dependent upon T_c. Three T_c regions are identified for different crystal orientations. Namely, the *c* axes in the PEO crystals are randomly oriented in the HPL structure when T_c < −50 °C. The *c* axes in the PEO crystals are preferentially oriented parallel to the {000*l*} of the HPL structure between −50 °C ≤ T_c ≤ −10 °C. The *c* axes in the PEO crystals are preferentially oriented inclined to the layer plane of the HPL structure between 0 °C ≤ T_c ≤ 40 °C. With increasing the T_c, the tilt angle of the *c* axes with respect to the {000*l*} layer plane gradually increases and finally reaches a plateau value of ∼60° at high T_cs. Perpendicular crystal orientation of the *c* axes with respect to the layer plane is not observed in this HPL confinement. At relatively low T_c < 0 °C, the PEO crystals are "confined" in the hexagonal compartments

of the PS perforations in the PEO layers, due to the impingements with neighboring crystals and/or PS perforations (i.e., a high nucleation density). Between 0 °C ≤ T_c ≤ 40 °C, the ribbonlike PEO lamellar crystals are tailored to grow in 1D along the {10$\bar{1}$0} planes of the PS perforations within the PEO layer due to low nucleation densities. The crystal orientation is found to occur in the early stage of crystallization with a crystallinity of ∼7 wt % and is determined by the crystal growth as evidenced from the self-seeded crystallization experiment. There are some interesting implications from these results. First, the covalent connectivity between the PS and PEO blocks in the block copolymer sample must play an important role in lowering the crystallinity of the PEO blocks (∼30% lower) compared with the PEO homopolymer fraction having the identical molecular weight. Second, the primary nucleation must not occur at the interfaces between the PS and PEO domanins; rather, the primary nuclei must be floating in the PEO layers as demonstrated in the self-seeding experiment. However, these logical implications need to be further verified in future experimental observations.

Acknowledgment. This work was supported by DMR of NSF. The simultaneous SAXS and WAXS experiments were carried out at the National Synchrotron Light Source at Brookhaven National Laboratory supported by the Department of Energy (DOE).

References and Notes

(1) Muthukumar, M.; Ober, C. K.; Thomas, E. L. *Science* **1998**, *277*, 1225.
(2) Zhu, L.; Chen, Y.; Zhang, A.; Calhoun, B. H.; Chun, M.; Quirk, R. P.; Cheng, S. Z. D.; Hsiao, B. S.; Yeh, F.; Hashimoto, T. *Phys. Rev. B* **1999**, *60*, 10022.
(3) Floudas, G.; Vazaiou, B.; Shipper, F.; Ulrich, R.; Wiesner, U.; Iatrou, H.; Hadjichristidis, N. *Macromolecules* **2001**, *34*, 2947.
(4) Reiter, G.; Castelein, G.; Hoerner, P.; Riess, G.; Sommer, J. U.; Floudas, G. *Eur. Phys. J. E* **2000**, *2*, 319.
(5) Chen, H.-L.; Wu, J.-C.; Lin, T.-L.; Lin, J.-S. *Macromolecules* **2001**, *34*, 6936.
(6) Hong, S.; Yang, L. Z.; MacKnight, W. J.; Gido, S. P. *Macromolecules* **2001**, *34*, 7009.
(7) Rohadi, A.; Endo, R.; Tanimoto, S.; Sasaki, S.; Nojima, S. *Polym. J.* **2000**, *32*, 602.
(8) Nojima, S.; Kato, K.; Yamamoto, S.; Ashida, T. *Macromolecules* **1992**, *25*, 2237.
(9) Ishikawa, S.; Ishizu, K.; Fukutomi, T. *Eur. Polym. J.* **1992**, *28*, 1219.
(10) Rangarajan, P.; Register, R. A.; Fetters, L. J.; Bras, W.; Naylor, S.; Ryan, A. J. *Macromolecules* **1995**, *28*, 4932.
(11) Ryan, A. J.; Hamley, I. W.; Bras, W.; Bates, F. S. *Macromolecules* **1995**, *28*, 3860.
(12) Ryan, A. J.; Fairclough, J. P. A.; Hamley, I. W.; Mai, S. M.; Booth, C. *Macromolecules* **1997**, *30*, 1723.
(13) Mai, S, M.; Fairclough, J. P. A.; Viras, K.; Gorry, P. A.; Hamley, I. W.; Ryan, A. J.; Booth, C. *Macromolecules* **1997**, *30*, 8392.
(14) Fairclough, J. P. A.; Mai, S.-M.; Matsen, M. W.; Bras, W.; Messe, L.; Turner, S. C.; Gleeson, A. J.; Booth, C.; Hamley, I. W.; Ryan, A. J. *J. Chem. Phys.* **2001**, *114*, 5425.
(15) Loo, Y.-L.; Register, R. A.; Ryan, A. J.; Dee, G. T. *Macromolecules* **2001**, *34*, 8968.
(16) Hamley, I. W.; Fairclough, J. P. A.; Bates, F. S.; Ryan, A. J. *Polymer* **1998**, *39*, 1429.
(17) Cohen, R. E.; Cheng, P. L.; Douzinas, K. C.; Kofinas, P.; Berney, C. V. *Macromolecules* **1990**, *23*, 324.
(18) Douzinas, K. C.; Cohen, R. E. *Macromolecules* **1992**, *25*, 5030.
(19) Cohen, R. E.; Bellare, A.; Drzewinski, M. A. *Macromolecules* **1994**, *27*, 2321.
(20) Liu, L. Z.; Yeh, F.; Chu, B. *Macromolecules* **1996**, *29*, 5336.
(21) Hamley, I. W.; Fairclough, J. P. A.; Terrill, N. J.; Ryan, A. J.; Lipic, P. M.; Bates, F. S.; Towns-Andrews, E. *Macromolecules* **1996**, *29*, 8835.
(22) Hamley, I. W.; Fairclough, J. P. A.; Ryan, A. J.; Bates, F. S.; Towns-Andrews, E. *Polymer* **1996**, *37*, 4425.
(23) Zhu, L.; Cheng, S. Z. D.; Calhoun, B. H.; Ge, Q.; Quirk, R. P.; Thomas, E. L.; Hsiao, B. S.; Yeh, F.; Lotz, B. *J. Am. Chem. Soc.* **2000**, *122*, 5957.
(24) Zhu, L.; Cheng, S. Z. D.; Calhoun, B. H.; Ge, Q.; Quirk, R. P.; Thomas, E. L.; Hsiao, B. S.; Yeh, F.; Lotz, B. *Polymer* **2001**, *42*, 5847.
(25) Zhu, L.; Calhoun, B. H.; Ge, Q.; Quirk, R. P.; Cheng, S. Z. D.; Thomas, E. L.; Hsiao, B. S.; Yeh, F.; Liu, L.; Lotz, B. *Macromolecules* **2001**, *34*, 1244.
(26) Weimann, P. A.; Hajduk, D. A.; Chu, C.; Chaffin, K. A.; Brodil, J. C.; Bates, F. S. *J. Polym. Sci., Polym. Phys. Ed.* **1999**, *37*, 2053.
(27) Kofinas, P.; Cohen, R. E. *Macromolecules* **1994**, *27*, 3002.
(28) Quiram, D. J.; Register, R. A.; Marchand, G. R. *Macromolecules* **1997**, *30*, 4551.
(29) Quiram, D. J.; Register, R. A.; Marchand, G. R.; Ryan, A. J. *Macromolecules* **1997**, *30*, 8338.
(30) Quiram, D. J.; Register, R. A.; Marchand, G. R.; Adamson, D. H. *Macromolecules* **1998**, *31*, 4891.
(31) Loo, Y. L.; Register, R. A.; Ryan, A. J. *Phys. Rev. Lett.* **2000**, *84*, 4120.
(32) Lotz, B.; Kovacs, A. J. *Kolloid Z. Z. Polym.* **1966**, *209*, 97.
(33) Lotz, B.; Kovacs, A. J.; Bassett, G. A.; Keller, A. *Kolloid Z. Z. Polym.* **1966**, *209*, 115.
(34) Kovacs, A. J.; Lotz, B.; Keller, A. *J. Macromol. Sci., Phys.* **1969**, *B3* (3), 385.
(35) Hirata, E.; Ijitsu, T.; Hashimoto, T.; Kawai, H. *Polymer* **1975**, *16*, 249.
(36) Yang, Y.-W.; Tanodekaew, S.; Mai, S.-M.; Booth, C.; Ryan, A. J.; Bras, W.; Viras, K. *Macromolecules* **1995**, *28*, 6029.
(37) Séguéla, R.; Prud'homme, J. *Polymer* **1989**, *30*, 1446.
(38) Park, C.; De Rosa, C.; Fetters, L. J.; Thomas, E. L. *Macromolecules* **2000**, *33*, 7931.
(39) Loo, Y. L.; Register, R. A.; Adamson, D. H. *Macromolecules* **2000**, *33*, 8361.
(40) Viras, F.; Luo, Y.-Z.; Viras, K.; Mobbs, R. H.; King, T. A.; Booth, C. *Makromol. Chem.* **1988**, *189*, 459.
(41) Hamley, I. W.; Wallwork, M. L.; Smith, D. A.; Fairclough, J. P. A.; Ryan, A. J.; Mai, S.-M.; Yang, Y. W.; Booth, C. *Polymer* **1998**, *39*, 3321.
(42) Hillmyer, M. A.; Bates, F. S. *Macromol. Symp.* **1997**, *117*, 121.
(43) Huang, P.; Zhu, L.; Calhoun, B. H.; Ge, Q.; Quirk, R. P.; Cheng, S. Z. D.; Thomas, E. L.; Hsiao, B. S.; Yeh, F.; Liu, L.; Lotz, B. *Macromolecules* **2001**, *34*, 6649.
(44) Zhu, L.; Huang, P.; Cheng, S. Z. D.; Ge, Q.; Quirk, R. P.; Thomas, E. L.; Lotz, B.; Wittmann, J.-C.; Hsiao, B. S.; Yeh, F.; Liu, L. *Phys. Rev. Lett.* **2001**, *86*, 6030.
(45) Alexander, L. E. *X-ray Diffraction Methods in Polymer Science*; Wiley-Interscience: New York, 1969.
(46) Takahashi, Y.; Tadokoro, H. *Macromolecules* **1973**, *6*, 672.
(47) Spontak, R. J.; Smith, S. D.; Ashraf, A. *Macromolecules* **1993**, *26*, 956.
(48) Chen, J.; Cheng, S. Z. D.; Wu, S. S.; Lotz, B.; Wittmann, J.-C. *J. Polym. Sci., Polym. Phys. Ed.* **1995**, *33*, 1851.
(49) Kovacs, A. J.; Straupe, C.; Gonthier, A. *J. Polym. Sci., Polym. Symp.* **1977**, *59*, 31.
(50) Koutsky, J. A.; Walton, A. G.; Baer, E. *J. Appl. Phys.* **1967**, *38*, 1832.

MA012184N